Applied Physics Letters ARTICLE scitation.org/journal/apl

Pressure-directed mixed ionic–electronic to pure electronic conduction transition and enhanced grain boundary conductivity in solid electrolyte $CdMoO_4$

Cite as: Appl. Phys. Lett. **121**, 112102 (2022); doi: 10.1063/5.0102805
Submitted: 13 June 2022 · Accepted: 23 August 2022 ·
Published Online: 12 September 2022

Tianru Qin,[1,2,3] Susu Duan,[2] Donghui Yue,[1,3] Jianfu Li,[4] Qinglin Wang,[2,a)] Fangxu Wang,[5] Weiwei Chen,[1] Xiaoli Wang,[4,a)] Youjin Zheng,[1,a)] and Chunxiao Gao[6]

AFFILIATIONS

[1]Heilongjiang Province Key Laboratory of Superhard Materials, Department of Physics, Mudanjiang Normal University, Mudanjiang 157012, China
[2]Shandong Key Laboratory of Optical Communication Science and Technology, School of Physics Science & Information Technology, Liaocheng University, Liaocheng 252059, China
[3]Center for High Pressure Science & Technology Advanced Research, Beijing 100094, China
[4]School of Physics and Electronic Information, Yantai University, Yantai 264005, China
[5]School of Physics and Electronic Engineering, Linyi University, Linyi 276005, China
[6]State Key Laboratory of Superhard Materials, Jilin University, Changchun 130012, China

[a)]**Authors to whom correspondence should be addressed:** zyjmsy@163.com; wangqinglin@lcu.edu.cn; and xlwang@ytu.edu.cn

ABSTRACT

Scheelite ABO_4-type solid electrolytes have attracted much attention for potential applications as oxygen ionic conductors of solid oxide fuel cells. Herein, a systematic study was carried out on the electrical transport properties of $CdMoO_4$ under high pressure by impedance spectroscopy measurements and theoretical calculations. The sequence of structural phase transitions at pressures was determined as $I4_1/a \rightarrow C2/c \rightarrow P2_1/c$ by the Crystal structure AnaLYsis by Particle Swarm Optimization (CALYPSO) method. A pressure-induced conduction transition from mixed ionic–electronic to pure electronic conduction was observed. Below 25.6 GPa, O^{2-} ions play a major role in the electrical transport process. The microscopic transport mechanism was analyzed with grain boundary energies and migration energy barriers. Above 26.9 GPa, the grain boundary response was weakened significantly after a pressure cycle, and the grain boundary conductivity increased by about three times due to pressure. These results provide guidelines for the optimization and application of scheelite ABO_4-based oxygen ionic conductors in solid oxide fuel cells.

Energy resources and materials are important for society to achieve sustainable development, and their exploration and research has become an important frontier scientific issue. Solid oxide fuel cells (SOFCs) are a clean energy technology that can efficiently convert chemical energy into electric energy by means of a chemical reaction.[1,2] Oxygen ionic conductor electrolyte materials are a key component of SOFCs,[3–5] and their properties (such as crystal structure, ionic conductivity, and grain boundary effects) directly affect the performance of the SOFC. Therefore, researchers are constantly searching for improved oxygen ionic conductors.

Scheelite ABO_4-type compounds possess a variety of excellent physical properties, and they have important applications as ionic conductors, microwave dielectric devices, solid-state lasers, and so on.[6–9] In their crystal structure, A and O atoms have various coordination forms in different systems, but each B atom is always surrounded by four O atoms in an approximately tetrahedral symmetry with a BO_4 configuration.[10,11] The tetrahedral anion in the scheelite structure has great deformation and rotation flexibility, making it a potential oxygen ionic conductor for SOFCs.[12–14]

At present, doping is the most common method used to optimize the performance of oxygen ionic conductors in SOFCs. Various substituted scheelite-type samples have been prepared by the solid-state reaction, and some new types of ionic conductors are found in scheelite-type solid solutions.[14–16] For example, bismuth vanadate

($BiVO_4$) has been reported with mixed oxygen ionic and electronic conductive behavior, and its conductivity and ionic transference numbers have been analyzed.[17,18] More recently, Yang *et al.* substituted Bi^{3+} with Sr^{2+} in $BiVO_4$ to obtain $Bi_{1-x}Sr_xVO_{4-0.5x}$.[14] Their theoretical and experimental results showed that the scheelite structure was able to incorporate oxygen vacancies or interstitial defects to facilitate high oxide ion migration. Although doping can improve the conductivity of oxygen ionic conductors, it can cause other problems such as formation of space charge layers that reduce grain boundary conductivity and resulting material properties. In addition to doping, pressure is an effective means to regulate the crystal structure and properties of materials. Under high pressure, ion interactions and grain boundary changes will inevitably affect the transport behavior of carriers.[19,20] Furthermore, the study of grain boundary transport processes under high pressure also helps reveal the mechanism of grain boundary effects on the functional properties of materials.

Cadmium molybdate ($CdMoO_4$) is a representative sample of the scheelite ABO_4 with a similar crystal structure to $BiVO_4$.[21,22] Jayaraman *et al.*[23] investigated the crystal structure of $CdMoO_4$ at pressures over 40 GPa by high-pressure Raman spectroscopy with a 4:1 methanol–ethanol mixture as pressure medium, revealing two phase transitions at 12 and 25 GPa. Shieh *et al.*[24] carried out high-pressure x-ray diffraction on $CdMoO_4$ without a pressure medium and determined the phase transition path from the initial tetragonal scheelite structure to the monoclinic wolframite structure and then to another phase with $BaWO_4$-II structure ($I4_1/a \rightarrow P2/c \rightarrow P2_1/n$). Errandonea *et al.*[25] studied the high-pressure structure of $CdMoO_4$ using angle-dispersive x-ray diffraction with a methanol–ethanol mixture as pressure medium. They reported a reversible phase transition from the scheelite structure to the *M*-fergusonite structure at 10.8 GPa ($I4_1/a \rightarrow I2/a$). The phase transition path between these works is inconsistent[23–25] and the research on $CdMoO_4$ electrical transport properties scarcely tackled, which limits the development and application of scheelite-based oxygen ionic conductors in SOFCs.

This work conducted *in situ* alternate-current (AC) impedance spectroscopy on $CdMoO_4$ in a diamond anvil cell up to 29.9 GPa. It explores the electrical transport process and distinguishes between contributions from the bulks vs grain boundaries. Electrical transport properties, including ionic and electronic conductivity, ionic diffusion coefficient, transference number, and relaxation frequency under high pressure, are discussed, and theoretical calculations provide the sequence of phase transitions under compression. The relationship between macroscopic electrical properties and microscopic crystal structure was further analyzed by theoretical calculations.

Figure 1 shows selected 3D perspective plots of $CdMoO_4$ impedance at different pressures up to 29.9 GPa. From 1.5 to 25.6 GPa, a semicircle arc appears in the high-frequency region on the left side of the Nyquist plots (Z' vs Z''), while Z'' increases with Z' in the low-frequency region on the right side. The high-frequency and low-frequency regions correspond to bulk and grain boundary responses, respectively.[26,27] In this pressure range, the semicircle arc corresponding to grain boundaries does not appear completely. It disappears above 26.9 GPa, leaving only the bulks' signal; this indicates that the electrical transport process is dominated by the bulks.

Bode plots (Z'' vs frequency) are mainly used to analyze relaxation phenomenon. Below 25.6 GPa, the peak in the high-frequency region corresponds to the bulk relaxation process and the grain boundary relaxation peak in the low-frequency region is not fully detected. Above 26.9 GPa, the grain boundary relaxation peak disappears. In Bode plots, the intensity variation and peak position reflect

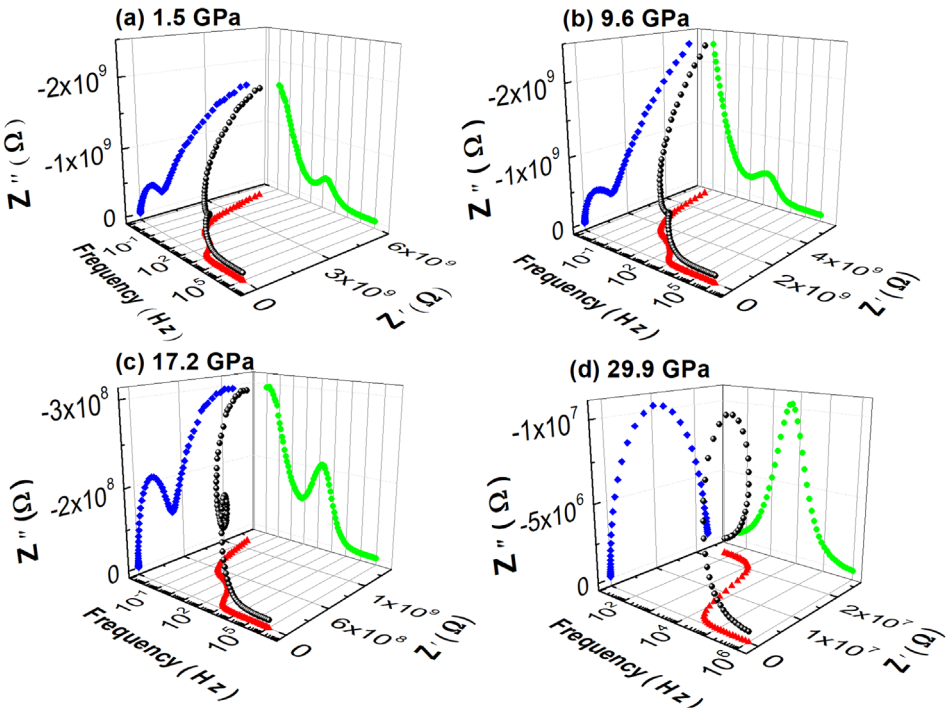

FIG. 1. Selected 3D impedance spectra (Z', Z'', and frequency) of $CdMoO_4$ at different pressures: (a) 1.5, (b) 9.6, (c) 17.2, and (d) 29.9 GPa. Black (3D curves of Z', Z'', and frequency), blue (Z', Z''), green (frequency, Z''), and red (frequency, Z'). The Z'' vs Z' as a Nyquist plot and the Z'' vs frequency as a Bode plot. See Fig. S1 for the impedance datasets.

the relaxation process under compression. From 1.5 to 6.8 GPa, the intensity of the bulk relaxation peak in the high-frequency region increases with increasing pressure. However, from 8.2 to 29.9 GPa, the intensity decreases, indicating that the bulk relaxation process is impeded by pressures above 8.2 GPa.

In addition to distinguishing between contributions from the bulks and from grain boundaries, impedance spectroscopy can also determine the conduction mechanism, such as electronic conduction, ionic conduction, or mixed ionic–electronic conduction. Warburg plots of impedance (Z' and $\omega^{-1/2}$) were adopted to analyze the conduction mechanism (Fig. S2).[28] Below 25.6 GPa, the linear relationship between Z' and $\omega^{-1/2}$ at low frequencies reflects the ionic diffusion behavior of $CdMoO_4$. Combined with the results in the Nyquist plots of Fig. 1, below 25.6 GPa, the signal corresponding to the grain boundaries in the low-frequency region is a curve with a visible arc, rather than a straight line with a slope of 45°. It can be concluded that the conduction mechanism of $CdMoO_4$ below 25.6 GPa is mixed ionic–electronic conduction. Ionic diffusion disappears above 26.9 GPa, and the mechanism changes to pure electronic conduction.

Based on the electrical conduction mechanism, carrier type, and grain boundary effects, two equivalent circuit models can be used to fit the impedance spectra (Fig. 2). The transport process of impedance includes non-Faradic and Faradic processes. The Faradic process is a charge–discharge process represented by a constant phase angle element (CPE). For electronic transport, the process is represented by a pure resistance (R_e); for ionic transport, it is represented by a resistance (R_i) and a Warburg element (W) in series in the equivalent circuit. For mixed ionic–electronic conduction, electronic and ionic transports are in a parallel relationship in the equivalent circuit. The Warburg impedance disappeared above 26.9 GPa, and the electrical transport was dominated by the bulks. The equivalent circuit can be simplified into a R_b-CPE_b parallel circuit. The simulated results are in good agreement with the experimental data (Fig. 2), indicating the validity of the selected equivalent circuits.

By fitting the impedance spectra, the pressure dependence of electronic and ionic conductivity of bulks and grain boundaries (σ_{be}, σ_{bi}, σ_{gbe}, and σ_{gbi}) are quantified in Figs. 3(a) and 3(b). Below 25.6 GPa, ionic conductivity is always higher than electronic conductivity, indicating that O^{2-} ions play a major role in mixed ionic–electronic conduction. The inflection points of the conductivity at 8.2 and 26.9 GPa are related to the previous reported pressure-induced structural phase transitions at 12 and 25 GPa, respectively.[24] A conduction transition from mixed ionic–electronic to pure electronic conduction is observed accompanying the second phase transition.

The swarm intelligence CALYPSO (Crystal structure AnaLYsis by Particle Swarm Optimization) method was used to explore the high-pressure structure of $CdMoO_4$ within the pressure range of 0–60 GPa and analyze enthalpy curves (relative to the $P2/c$ structure) of various $CdMoO_4$ structures as a function of pressure (Fig. S3). The sequence of phase transitions under compression was determined as $I4_1/a \rightarrow C2/c \rightarrow P2_1/c$. The phonon dispersion curves of $CdMoO_4$ at 0, 5, and 45 GPa were calculated (Fig. S4) and indicate that the dynamics of the high-pressure phases are stable. For convenience, the three phases—$I4_1/a$, $C2/c$, and $P2_1/c$—are herein referred to as phase I, phase II, and phase III, corresponding to the pressure ranges of 1.5–6.8, 8.2–25.6, and 26.9–29.9 GPa in the experiment, respectively. There are differences between our theoretical results and previous

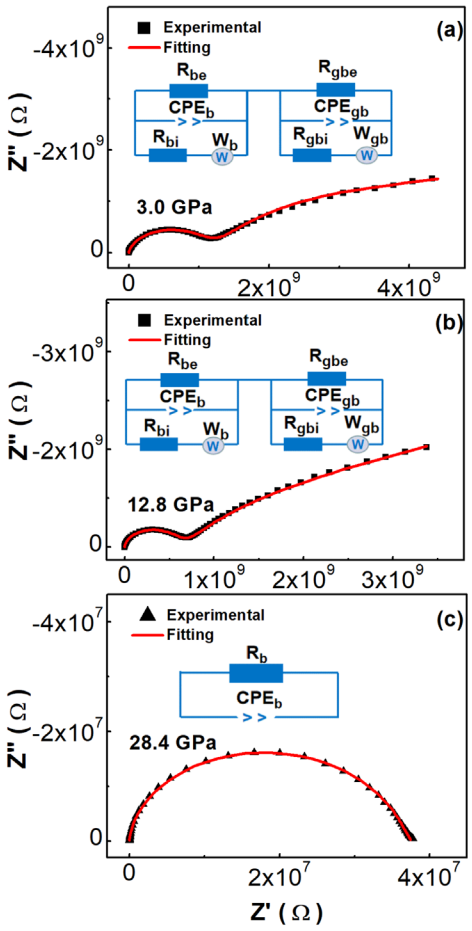

FIG. 2. Equivalent circuit diagrams and selected fitting results for (a) mixed ionic–electronic conduction at 3.0 GPa, (b) mixed ionic–electronic conduction at 12.8 GPa, and (c) electronic conduction at 28.4 GPa in $CdMoO_4$. R, CPE, and W are the resistance, constant phase angle element, and Warburg impedance of ion diffusion, respectively. Subscripts b, gb, e, and i denote bulk, grain boundary, electronic, and ionic, respectively.

experimental results,[23–25] which may be related to the hydrostatic pressure environment; the shear stress generated by nonhydrostatic pressure may affect the phase transition path.[29–31]

The bulk electronic conductivity (σ_{be}) at different pressures is shown in Fig. 3(a). To further analyze the conductivity, the bandgap was calculated (Fig. S5) and found to decrease with increasing pressure in all three phases. Conductivity would normally increase with a narrowing bandgap. However, it is also affected by the electronic transference number (t_e), which represents the concentration of electrons involved in conduction and is positively correlated with σ_{be}. As shown in Fig. 3(d), t_e decreases with pressure in phase I but increases in phase II. The decreased σ_{be} in phase I is due to the decreased t_e, while the increased σ_{be} in phase II is caused by the narrowed bandgap and increased t_e. In phase III, the conduction mechanism changes to pure electronic conduction, and the increased σ_{be} can be attributed to the narrowed bandgap.

Ionic conductivity is closely related to the ionic diffusion coefficient, the ionic transference number, and the carrier mobility. Both the

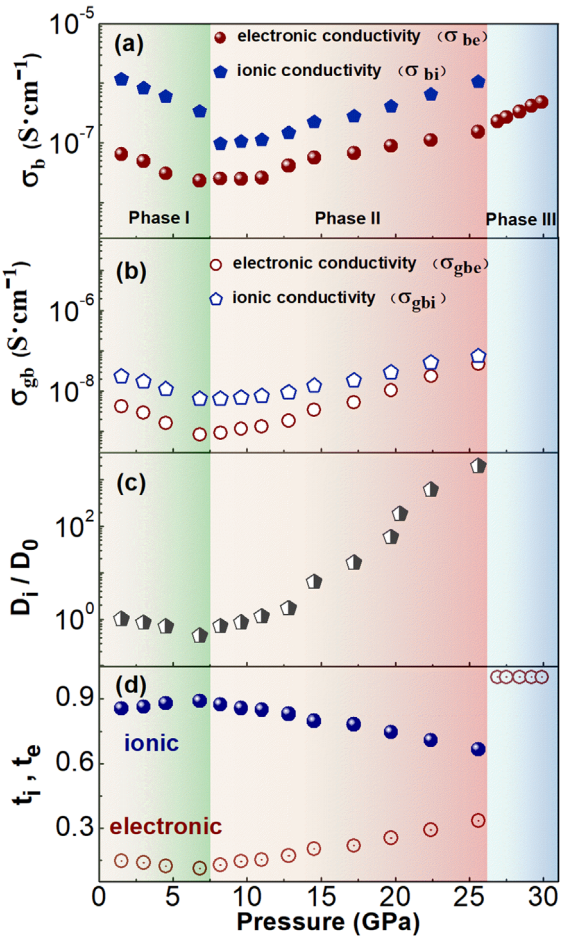

FIG. 3. Relationships of electronic and ionic conductivity of (a) bulks and (b) grain boundaries (σ_{be}, σ_{bi}, σ_{gbe}, σ_{gbi}); (c) the relative ionic diffusion coefficient (D_i/D_0); and (d) the ionic and electronic transference number (t_i, t_e) vs pressure for $CdMoO_4$. D_0 represents the diffusion coefficient at 1.5 GPa. The above parameters are derived from the impedance data (see the supplementary material for details).

diffusion coefficient and mobility characterize the speed of carrier migration, and there is a proportional Einstein relation between the two parameters.[32] Therefore, the diffusion coefficient can also qualitatively reflect the change of mobility. Based on the impedance spectra, calculations were made for the relative ionic diffusion coefficient (D_i/D_0) and the transference number of O^{2-} ions (t_i) and electrons (t_e); these results are shown in Figs. 3(c) and 3(d).[28,33]

In phase I, the bulk ionic conductivity (σ_{bi}) and D_i/D_0 decrease with increasing pressure while t_i increases (Fig. 3). This indicates that, while the concentration of ions involved in conduction increased, the ionic diffusion became more difficult. This may be related to the energy barrier for carrier transport. The calculated migration energy barriers of O^{2-} ions along the path from sites *a* to site *g* at different pressures in phase I are shown in Figs. 4(a) and 4(d). Migration barrier energies increase with increasing pressure, indicating that ionic diffusion becomes more difficult. Although the ionic transference number increased in phase I, bulk ionic conductivity still decreases with increasing pressure. The choice of O^{2-} migration path is based on the principle of minimum energy barrier. This is along the *z* direction for phases I and II and along the *y* direction for phase III. It should be noted that migration along the selective direction is not the only path. If there is a strong enough voltage in other directions that can overcome the barrier, resulting in the migration of O^{2-}.

In phase II, both σ_{bi} and D_i/D_0 increase with increasing pressure while t_i decreases (Fig. 3). The calculated O^{2-} ions migration energy pathway for phase II is shown in Figs. 4(b) and 4(e), decreasing from 3.279 eV at 10 GPa to 3.123 eV at 30 GPa. Although the ionic concentration decreases with increasing pressure, the reduced energy barriers promote bulk ionic conduction and diffusion becomes easier. This explains why the diffusion coefficient increases by three orders of magnitude at 25.6 GPa, although ionic conductivity increases by only one order of magnitude. In phase III [Figs. 4(c) and 4(f)], although the migration barrier energy decreases with increasing pressure, ionic transference number is minimal [Fig. 3(d)], and the transport process is dominated by the electron conduction.

To better understand carrier transport at grain boundaries, the grain boundary energy with selected grain boundary planes in each phase was calculated and is shown as Fig. 5. In general, the grain boundary energy consists of the elastic distortion energy, which depends on the degree of misorientation, and chemical interaction energy, which depends on the chemical bonding of atoms on the grain boundary. As shown in Figs. 5(b)–5(d), the bonding of atoms at the grain boundary does not obviously change in different phases. Therefore, the grain boundary energy is mainly a function of elastic distortion. The variation of grain boundary energy with pressure reflects the degree of misorientation in the grain boundary, which can also be understood as the variation of grain boundary density.

As shown in Fig. 5(a), for phase I, the rapidly increasing grain boundary energy with pressure indicates that the degree of misorientation also increases rapidly with pressure, enhancing the scattering effect of grain boundary on carriers. The electronic transference number and ionic diffusion coefficient decrease, and the ionic transference number increases, with increasing pressure in phase I [Fig. 3(d)]. Therefore, the electronic and ionic conductivities of the grain boundary (σ_{gbe} and σ_{gbi}, respectively) decrease with increasing pressure in phase I [Fig. 3(b)]. For phase II, the grain boundary energy still increases with pressure, but the rate of increase is slower. The effect of the increasing electronic transference number is stronger than the increasing degree of misorientation, so σ_{gbe} increases. The ionic transference number decreases with increasing pressure in phase II, but the ionic diffusion coefficient increases. Similarly, the diffusion effect is stronger than the increased degree of misorientation, resulting in an increased σ_{gbi} with increasing pressure in phase II. For phase III, the grain boundary energy is obviously lower than that of phases I and II, which indicates that the misorientation of the grain boundary is small and the grain boundary effect is weakened. Therefore, the bulk dominates the electrical transport process.

The bulk relaxation frequency and the relative permittivity were also analyzed [Figs. S6(a) and S6(b)]. According to the Arrhenius relationship,[34] the pressure dependences of the activation energy in phases I, II, and III was calculated to be 2.56, −2.74, and −12.31 meV/GPa, respectively. In phase I, the increased relaxation activation energy indicates that the vibration damping of the Mo–O dipole increases and the charge–discharge rate slows down. However, the relaxation activation

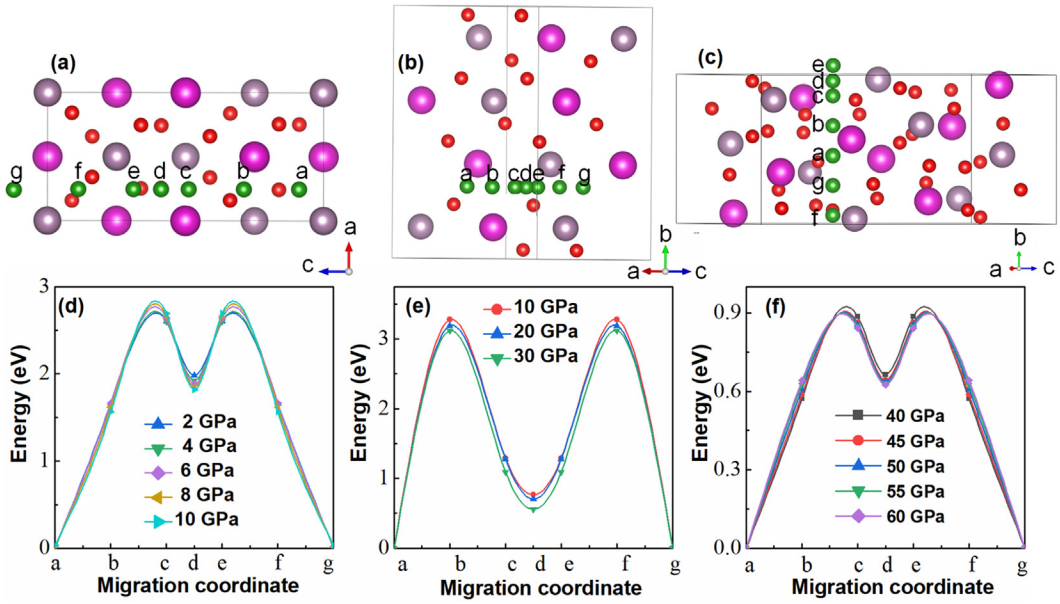

FIG. 4. (a)–(c) Crystal structures of (a) phase I, (b) phase II, and (c) phase III; pink, gray, and red spheres represent Cd, Mo, and O atoms, respectively. Green spheres show the minimum energy path for O^{2-} ions from sites *a* to site *g*. (d)–(f) Calculated energy barriers of O^{2-} ions migration in (d) phase I, (e) phase II, and (f) phase III along the minimum energy path at different pressures.

energies in phases II and III are negatively correlated with pressure, indicating that the charge–discharge process becomes easier. As pressure increases, the relative permittivity decreases in phases I and III but increases in phase II. The variation of relative permittivity indicates that the dielectric performance of $CdMoO_4$ can be modulated by pressure.

Nyquist plots and dielectric loss for compressed (at 1.5 GPa) and decompressed (at 1.4 GPa) systems are compared in Figs. S6(c) and S6(d). Note that the grain boundary response was obviously weakened after a pressure cycle. When pressure was released to 1.4 GPa, the grain boundary ionic conductivity (σ_{gbi}) was 7.8×10^{-8} S cm and the electronic conductivity (σ_{gbe}) was 1.2×10^{-8} S cm. Compared with a pressure of 1.5 GPa during compression, grain boundary conductivity increased by about three times after a pressure cycle. This suggests that pressure can effectively improve the grain boundary conductivity of oxygen ionic conductors. Since the bulk response returns to its initial state after a pressure cycle, the different dielectric loss between compressed and decompressed materials is mainly due to the pressure-induced microstructural grain boundary rearrangement. Therefore, the grain boundary effect of $CdMoO_4$ can be effectively regulated by pressure.

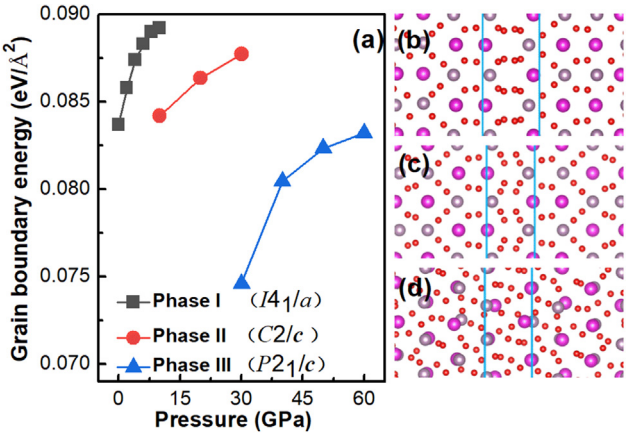

FIG. 5. (a) Grain boundary energies of different phases under compression; (b) (001)(00$\bar{1}$) grain boundary for phase I; (c) (010)(0$\bar{1}$0) grain boundary for phase II; and (d) (001)(00$\bar{1}$) grain boundary for phase III. Pink, gray, and red spheres represent Cd, Mo, and O atoms, respectively. Blue lines indicate borders of the primitive grain boundary cells.

In summary, the electrical transport properties of $CdMoO_4$ were investigated up to 29.9 GPa by *in situ* AC impedance spectroscopy and theoretical calculations. Conduction transitioned from mixed ionic–electronic to pure electronic at 26.9 GPa, accompanied by a structural phase transition. In addition, the phase transition sequence under compression was given by the CALYPSO method. The contribution of the bulks and the grain boundaries was also distinguished. Below 25.6 GPa, ionic conductivity was higher than electronic conductivity. The variation of bulk ionic conductivity with pressure was related to the migration energy barrier, and the pressure dependence of the bulk electronic conductivity was due to the variation of electronic concentration under compression. Carrier transport at grain boundaries was analyzed with grain boundary energy; the variation of relative permittivity under compression indicated that the dielectric performance could be modulated by pressure. Above 26.9 GPa, the bulk dominated the electrical transport process. After a pressure cycle, the grain boundary response weakened significantly, and the grain boundary conductivity increased by a factor of three. This work provides guidelines for designing and optimizing scheelite-based oxygen ionic conductors for SOFCs.

See the supplementary material for methods, impedance datasets, Z' vs $\omega^{-1/2}$ plots, derivations of conductive parameters from impedance data, calculated enthalpy, phonon dispersion curves and band gaps of predicted structures, and dielectric results.

This work was supported by Heilongjiang Provincial Education Department Project Subsidy (Grant Nos. 1451MSYYB006 and 1354MSYQN022), the Natural Science Foundation of Heilongjiang Province (Grant Nos. LH2021A021 and LH2019A024), the Research Funding of Mudanjiang Normal University (Grant Nos. GP2022003, YB2019009, MNUB201806, and MNUB201912), the Science and Technology Plan of Youth Innovation Team for Universities of Shandong Province (Grant No. 2019KJJ019), the Introduction and Cultivation Plan of Youth Innovation Talents for Universities of Shandong Province, the National Natural Science Foundation of China (Grant Nos. 11604133 and 11974154), the Open Project of Shandong Key Laboratory of Optical Communication Science and Technology (Liaocheng University, Grant No. SDOC201902), the Open Project of State Key Laboratory of Superhard Materials (Jilin University, Grant No. 202101), and the Research Funding of Liaocheng University (Grant Nos. 318012016, 318051610, and 318051612).

AUTHOR DECLARATIONS

Conflict of Interest

The authors have no conflicts to disclose.

Author Contributions

Tianru Qin: Conceptualization (lead); Formal analysis (lead); Investigation (lead); Writing – original draft (lead). **Chunxiao Gao:** Formal analysis (equal); Supervision (equal). **Susu Duan:** Investigation (equal); Validation (equal). **Donghui Yue:** Investigation (equal); Validation (equal); Visualization (equal). **Jianfu Li:** Investigation (equal); Validation (equal); Visualization (equal). **Qinglin Wang:** Conceptualization (equal); Supervision (equal); Writing – review & editing (equal). **Fangxu Wang:** Investigation (equal). **Weiwei Chen:** Investigation (equal). **Xiaoli Wang:** Formal analysis (equal); Software (equal); Writing – review & editing (equal). **Youjin Zheng:** Resources (equal); Supervision (equal); Writing – review & editing (equal).

DATA AVAILABILITY

The data that support the findings of this study are available within the article and its supplementary material.

REFERENCES

[1]A. Ndubuisi, S. Abouali, K. Singh, and V. Thangadurai, J. Mater. Chem. A **10**, 2196 (2022).
[2]W. Kong, Z. Han, S. Lu, and M. Ni, Appl. Energy **287**, 116586 (2021).
[3]A. P. Jamale, A. Natoli, and L. D. Jadhav, J. Phys. Chem. Solids **148**, 109723 (2021).
[4]B. Wang, N. Li, Y. Zhao, X. Liu, M. Li, Q. Zhang, H. Dong, Y. He, D. Zhang, Y. Wang, G. Liu, Y. Long, and W. Yang, Appl. Phys. Lett. **119**, 043902 (2021).
[5]M. Yashima, T. Tsujiguchi, Y. Sakuda, Y. Yasui, Y. Zhou, K. Fujii, S. Torii, T. Kamiyama, and S. J. Skinner, Nat. Commun. **12**, 556 (2021).
[6]T. Groń, E. Tomaszewicz, M. Berkowski, B. Sawicki, P. Urbanowicz, J. Kusz, H. Duda, and M. Oboz, Ceram. Int. **42**, 4185 (2016).
[7]S. Injac, A. K. L. Yuen, M. Avdeev, C. H. Wang, P. Turner, H. E. A. Brand, and B. J. Kennedy, Inorg. Chem. **59**, 2791 (2020).
[8]T. Qin, Q. Wang, D. Yue, H. Liu, T. Ji, Y. Han, Y. Zheng, and C. Gao, J. Phys. Chem. C **124**, 17932 (2020).
[9]S. Raghunath and R. Balan, Mater. Today: Proc. **46**, 2930 (2021).
[10]C. Tablero, Chem. Phys. Lett. **635**, 190 (2015).
[11]D. Errandonea and A. B. Garg, Prog. Mater. Sci. **97**, 123 (2018).
[12]T. Esaka, T. Mina-ai, and H. Iwahara, Solid State Ionics **57**, 319 (1992).
[13]J. Wang, L. Zhou, Y. Wang, J. Xu, X. Yang, and X. Kuang, J. Solid State Chem. **268**, 16 (2018).
[14]X. Yang, A. J. Fernández-Carrión, J. Wang, F. Porcher, F. Fayon, M. Allix, and X. Kuang, Nat. Commun. **9**, 4484 (2018).
[15]T. Esaka, Solid State Ionics **136–137**, 1–9 (2000).
[16]A. J. Weisentein, N. Childs, R. Amendola, D. Driscoll, S. W. Sofie, P. Gannon, and R. Smith, Mater. Chem. Phys. **139**, 706 (2013).
[17]K. Hirota, G. Komatsu, M. Yamashita, H. Takemura, and O. Yamaguchi, Mater. Res. Bull. **27**, 823 (1992).
[18]I. C. Vinke, J. Diepgrond, B. A. Boukamp, K. J. De Vries, and A. J. Burggraaf, Solid State Ionics **57**, 83 (1992).
[19]T. Qin, Q. Wang, D. Yue, H. Liu, Y. Zheng, Y. Han, and C. Gao, J. Alloys Compd. **814**, 152336 (2020).
[20]Q. Wang, X. Wang, J. Li, T. Qin, D. Sang, J. Liu, F. Ke, X. Wang, Y. Li, and C. Liu, J. Mater. Chem. C **9**, 4764 (2021).
[21]M. Isacfranklin, R. Yuvakkumar, G. Ravi, E. S. Babu, D. Velauthapillai, M. Thambidurai, C. Dang, T. S. Algarni, and A. M. Al-Mohaimeed, JOM **73**, 1546 (2021).
[22]B. Sawicki, E. Tomaszewicz, T. Groń, M. Berkowski, M. Głowacki, M. Oboz, J. Kusz, and S. Pawlus, J. Materiomics **7**, 845 (2021).
[23]A. Jayaraman, S. Y. Wang, and S. K. Sharma, Phys. Rev. B **52**, 9886 (1995).
[24]S. R. Shieh, L. C. Ming, and A. Jayaraman, J. Phys. Chem. Solids **57**, 205 (1996).
[25]D. Errandonea, D. Santamaria-Perez, S. N. Achary, A. K. Tyagi, P. Gall, and P. Gougeon, J. Appl. Phys. **109**, 043510 (2011).
[26]M. B. Ortuño-López, J. J. Valenzuela-Jáuregui, R. Ramírez-Bon, E. Prokhorov, and J. González-Hernández, J. Phys. Chem. Solids **63**, 665 (2002).
[27]T. B. Adams, D. C. Sinclair, and A. R. West, Phys. Rev. B **73**, 094124 (2006).
[28]Q. Wang, C. Liu, Y. Han, C. Gao, and Y. Ma, Rev. Sci. Instrum. **87**, 123904 (2016).
[29]D. Errandonea, L. Gracia, R. Lacomba-Perales, A. Polian, and J. C. Chervin, J. Appl. Phys. **113**, 123510 (2013).
[30]D. Errandonea, A. Muñoz, and J. Gonzalez-Platas, J. Appl. Phys. **115**, 216101 (2014).
[31]D. Errandonea, Cryst. Res. Technol. **50**, 729 (2015).
[32]A. Solon and J. M. Horowitz, J. Phys. A **55**, 184002 (2022).
[33]Q. Wang, C. Liu, Y. Gao, Y. Ma, Y. Han, and C. Gao, Appl. Phys. Lett. **106**, 132902 (2015).
[34]T. Qin, Q. Wang, D. Yue, W. Shen, Y. Yan, Y. Han, Y. Ma, and C. Gao, J. Alloys Compd. **730**, 1–6 (2018).